WPMST1-PR(18) 19970

M Carr et al.

Impact of ray-tracing techniques on bolometry inversions and total radiated power measurements at ASDEX Upgrade

Preprint of Paper to be submitted for publication in
Review of Scientific Instruments

This work has been carried out within the framework of the EUROfusion Consortium and has received funding from the Euratom research and training programme 2014-2018 under grant agreement No 633053. The views and opinions expressed herein do not necessarily reflect those of the European Commission.

Impact of ray-tracing techniques on bolometry inversions and total radiated power measurements at ASDEX Upgrade

M. Carr,[1, a)] A. Meakins,[1] M. Bernert,[2] P. David,[2] C. Giroud,[1] J. Harrison,[1] S. Henderson,[1] B. Lipschultz,[3] F. Reimold,[4] the EUROfusion MST1 Team,[b)] and ASDEX Upgrade team

[1)] *CCFE, Culham Science Centre, Abingdon, Oxon, OX14 3DB, UK*

[2)] *Max-Planck-Institut für Plasmaphysik, 85748 Garching, Germany.*

[3)] *York Plasma Institute, Department of Physics, University of York, Heslington, York, UK*

[4)] *Max-Planck-Institut für Plasmaphysik, Greifswald, Germany.*

(Dated: 27 March 2018)

Ray-tracing techniques are applied to bolometry, a diagnostic particularly sensitive to machine geometry due to the effect of the finite collection volume subtended by a 3D aperture. Sightlines from the ASDEX Upgrade bolometer foils were ray-traced with a path tracing algorithm, where the optical path is represented by a statistical bundle of ray paths connecting the foil surface with the slit geometry. By using the full 3D machine CAD model for the detector box and first wall, effects such as occlusion and vignetting were included in the calculation of the bolometer's étendue. Inversion matrices calculated with the ray-tracing technique were compared with the more conventional single-ray approach and shown to be naturally more constrained, requiring less regularisation and therefore less assumptions about the plasma's emissivity profile. Relative differences between reconstructed emissivity distributions from the two models are shown to be significant for a sample radiation scenario. The volume ray-tracing technique consistently outperformed the single-ray approach when inverting a population of emission phantoms, as measured by the correlation between the inversion and the solution. Consequences for the overall shape of the inverted radiation distribution and total radiated power are discussed in the context of our ability to measure these parameters with the required accuracy for ITER and DEMO. These results are particularly relevant for the divertor where strong emission gradients may be present.

I. INTRODUCTION

To protect the divertor components in machines on the scale of ITER and DEMO, a large fraction of the exhaust power entering the scrape of layer must be radiated before it reaches the divertor targets[1]. Multi-channel bolometry is a key diagnostic used in current experiments to facilitate the development of highly radiating divertor scenarios[2]. An accurate bolometric diagnostic is essential for both measuring the total radiated power fraction and determining the spatial distribution of the emissivity.

A bolometer is designed to effectively be a black surface such that it will absorb all photons incident upon it, yielding a measurement of the radiant flux at that surface. In practice, real materials will be absorbent in some wavelength regions and reflective in others. Gold is usually used as the material of choice because it exhibits strong absorption above $\sim$ 3eV, which corresponds well to the spectral region where the bulk of the power is radiated in a typical tokamak plasma[2]. Although some studies have suggested further blackening coatings should be added to extend the energy range of absorption to longer wavelengths[3].

The limited geometric accessibility around tokamak plasmas means most bolometry diagnostics are installed as fans of pinhole cameras at a low number of observation points. The plasma's local emissivity profile is then inferred from the line integrated measurements by means of standard tomography techniques[2,4]. Figure 1 shows the FLH bolometer camera in situ at ASDEX Upgrade (AUG).

The response of the collimated detectors is often modelled with the line-of-sight approximation, i.e. assuming views along infinitely thin straight lines, which will hereafter be referred to as the single-ray model. However, this approximation leads to aliasing effects and is a poor representation of the detector when the beam width is significantly larger than the inversion grid cells. The most advanced model was developed by Ingesson et. al.[5] and considers the response of an ideal rectangular pinhole and detector analytically. However this model still requires assumptions such as toroidal symmetry and doesn't take into account the 3D structure of the first wall.

The most complete numerical approach is to use Monte Carlo techniques to launch an ensemble of rays from the detector surface and trace them through to collisions with the as-built engineering model for detector aperture surfaces and the first wall. This process would result in a complete model of the coupling between the emission source and the detector including all 3D effects, such as occlusion and vignetting. Occlusion being when rays are obstructed by structures external to the camera (e.g. wall tiles), and vignetting being rays obstructed by the cam-

[a)] matthew.carr@ukaea.uk

[b)] See the author list of Meyer, H., et al. "Overview of progress in European medium sized tokamaks towards an integrated plasma-edge/wall solution." Nucl. Fusion (2017).

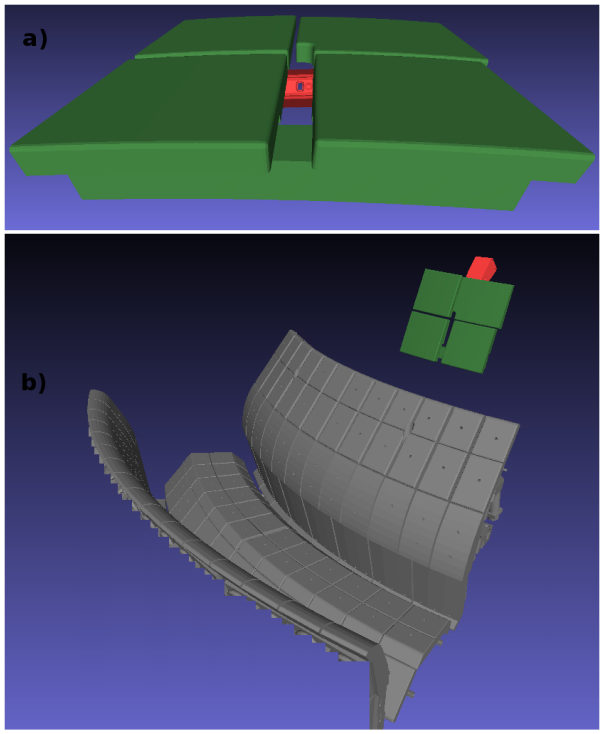

FIG. 1. a) Example visualisation of the FLH bolometer camera (red), which contains four bolometer foil sightlines, with its pinhole viewing between a first wall tile gap (green). In b) the same FLH camera is shown with its context viewing into the AUG divertor (grey). Note that the model detail has been reduced for visualisation.

era apperture. This Monte Carlo approach will be referred to as the volume ray-tracing technique.

The CHERAB code[6] was developed at JET as a platform for modelling spectroscopic diagnostics with the Raysect ray-tracing package[7]. Raysect is an open-source scientific ray-tracing framework that is capable of handling detailed 3D engineering geometry and physically accurate reflections. In this work CHERAB has been extended for use with bolometry by exploiting Raysect's Monte Carlo ray-tracing capabilities. The AUG bolometry system[8] was used as a case study diagnostic system for testing the relative benefits of the volume ray-tracing technique, although the conclusions should be generally applicable to other fusion devices.

II. RAY TRACING BOLOMETER MODEL

The total power (radiant flux) measured by an observing surface is given by the integral of the incident emission over the collecting solid angle Ω and surface area A.

$$\Phi = \int_A \int_\Omega L_i(\mathbf{x}, \omega) \times \cos(\theta) d\omega dA \tag{1}$$

Here, $L_i(\mathbf{x}, \omega)$ is the incident radiance arriving at a given point $\mathbf{x}$ and incident angle ω on the observing surface. The $\cos(\theta)$ term is a geometry factor describing the increase in effective observing area as the incident rays become increasingly parallel to the surface.

Equation 1 is exact, but extremely difficult to evaluate analytically for any realistic bolometer foil geometry and radiation distribution. In practice, it is easier to evaluate this integral with Monte Carlo integration and importance sampling which approximates the integral with a weighted average[9,10]. The Monte Carlo integral estimator for a function f takes the form

$$I \approx \frac{1}{N} \sum_{j=1}^{N} \frac{f(x_j)}{p(x_j)}. \tag{2}$$

with $f(x)$ evaluated at N sample points x_j and $p(x_j)$, given by

$$p(x_j) = \frac{q(x_j)}{\int q(x) dx}, \tag{3}$$

is the probability density function evaluated at the given sample point. $q(x)$ is the weight function for cases when the sample points are drawn from a non-uniform sample distribution.

The lighting integral in equation 1 can be naturally discretised in terms of N_r rays, composed of 2D sample points $\mathbf{x_j}$ on detector area A_d and sample vectors ω_j on the hemisphere Ω. Therefore, the estimator for the power arriving on a bolometer foil would take the form

$$\Phi \approx \frac{1}{N_r} \sum_{j=1}^{N_r} \frac{L_i(\mathbf{x_j}, \omega_j) \cos(\theta_j)}{p_A(\mathbf{x_j}) p_\Omega(\omega_j)}. \tag{4}$$

If the sample points are drawn uniformly over the detector area, then $p_A(\mathbf{x_j}) = 1/A_d$. The natural choice for sampling the vectors is a uniform hemisphere. However, for a bolometer detector the pinhole typically occupies a small solid angle leading to very computationally inefficient sampling. It is more efficient to sample the minimum cone of solid angle (with half angle θ_h) that tightly wraps the pinhole. If the vectors are generated uniformly over solid angle, the weighting function is still uniform, $q(\omega) = 1$, and thus the pdf takes on the form of the fractional solid angle, $p_\Omega(\omega_j) = 1/(2\pi(1 - \cos(\theta_h))) = 1/\Omega_{frac}$. The estimator becomes

$$\Phi \approx \frac{\Omega_{frac} A_d}{N_r} \sum_{j=1}^{N_r} L_i(\mathbf{x_j}, \omega_j) \cos(\theta_j). \tag{5}$$

III. ÉTENDUE CALCULATION

The étendue of the detector including occlusion and vignetting effects can be calculated by the weighted fraction of rays that pass through the slit multiplied by the full étendue that was sampled.

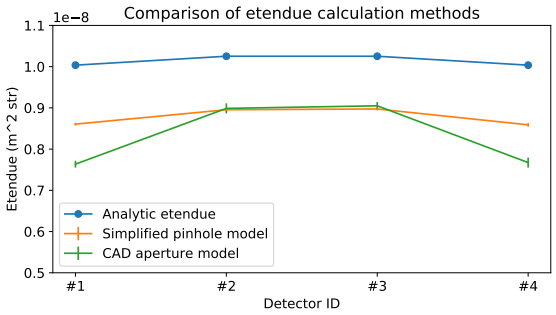

FIG. 2. The four foil detector étendues for the FLH camera were calculated with the analytic pinhole approximation (Eqn. 7) and these are compared with the ray-tracing étendue values (Eqn. 6). The three cases shown are a) the analytic pinhole approximation, b) the ray-tracing calculation with a realistic first wall model and a simplified pinhole in a rectangular plane, and c) as b) but also including the full as built detector geometry.

$$\epsilon_{det} = \frac{\Omega_{frac} A_d}{N_r} \sum_{j=1}^{N_r} \delta_j \cos(\theta_j), \quad \delta_j = \begin{cases} 0, & \text{ray hits} \\ 1, & \text{ray misses} \end{cases} \tag{6}$$

Here, ϵ_{det} has units of [m^2 str] and $\delta_j = 0$ if the jth ray hits any of the obstructing aperture surfaces, or $\delta_j = 1$ if the ray passes through unencombered to the plasma.

With this calculation the étendue for an arbitrary pinhole-foil geometry can be calculated to arbitrary precision with sufficient ray samples. By contrast, it is more common in bolometry to use the approximate pinhole formula[2,5]

$$\epsilon_{pin} = \frac{\cos(\gamma)\cos(\alpha) A_d A_p}{d^2}. \tag{7}$$

Where A_p is the rectangular pinhole area, d is the distance between the pinhole and detector, and γ, α are compound angles describing the orientation of the foil surface with respect to the pinhole axis[2,5].

The difference between the two étendue calculation methods was calculated for all AUG bolometer foils, an example calculation for the FLH camera is shown in Figure 2. The ray-tracing calculation was done with both b) a simplified and c) full detail aperture to separate out the different contributions. The simplified aperture used a rectangular plane with a rectangular pinhole cut out of the plane, whereas c) used the full detail engineering model of the as built detector.

There is a systematic offset between the analytic a) and ray-traced simple pinhole b) cases, which is likely due to the truncation of terms in the derrivation of the approximate étendue equation 7. The extra drop in etendue between b) and c) is due to vignetting effects at the edges of the camera field of view when the full CAD geometry is included. The étendue calculations for the FHC camera had an average deviation of 10.8% compared with the much smaller 2.7% on the FLX camera. It was found that each camera had a distinctly different mean deviation, which is likely due to differences in the camera geometry that have more or less effect on the assumptions in 7. These étendue deviations act as an extra systematic noise source in the inversion process.

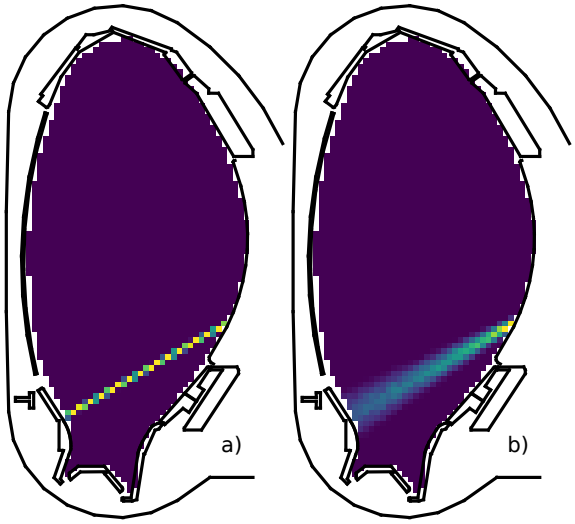

FIG. 3. Comparison of sensitivity matrices $\mathbf{W}$ in the poloidal plane for a bolometer foil modelled with a single-ray and a volume sampled light cone.

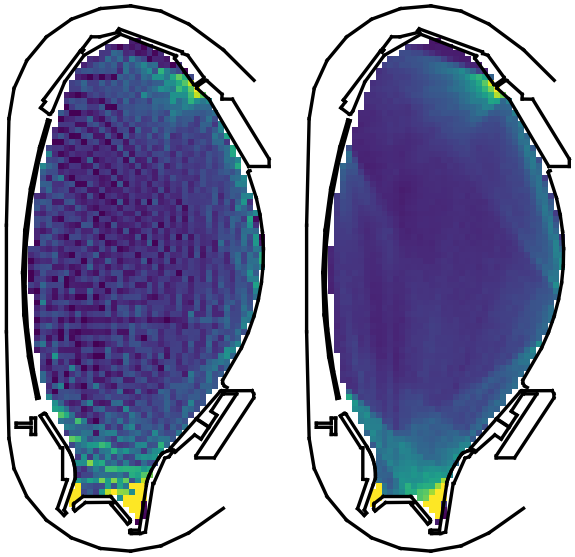

FIG. 4. Comparison of the sight line densities for foil bolometers at AUG modelled with single-ray paths and volume sampled light cones.

IV. SENSITIVITY MATRICES

Recovering the plasma emission with tomography is an ill-posed problem. It is customary to describe the system in terms of a sensitivity matrix $\mathbf{W}$. The elements $W_{k,l}$

describe the coupling between the N_s plasma emission sources x_l and measured power Φ_k at N_d detectors. The whole detector set is typically represented as the matrix equation

$$\mathbf{\Phi} = \mathbf{W}\mathbf{x}. \tag{8}$$

The power for the kth detector can be expressed as

$$\Phi_k = \sum_{l=1}^{N_s} W_{k,l} x_l, \tag{9}$$

where k and l are the indices for the detectors and sources respectively. Equation 8 can then be inverted using established tomography techniques[2,4] to yield the spatial emissivities from a measured set of power values.

The conventional analysis technique estimates the single ray sensitivity matrix $\mathbf{W_{SR}}$ by tracing a straight line through the system, originating at the centre of the detector surface and passing through the slit centre. Every sensitivity element $W_{k,l}$ is weighted by the length of the ray segment, $s_{k,l}$, that intersects with the lth emitting cell.

$$\mathbf{W_{SR}}: \quad W_{k,l} = s_{k,l} \times \epsilon_{pin} \tag{10}$$

In contrast, the ray-tracing technique launches N_r randomly generated rays from the detector and performs a weighted sum of the ray lengths, $s_{j,k,l}$, that intercept with the cell using equation 5. Rays that collide with the slit geometry or miss the cell have a zero weighting.

$$\mathbf{W_{Vol}}: \quad W_{k,l} = \frac{\Omega_{frac} A_d}{N_r} \sum_{j=1}^{N_r} s_{j,k,l} \cos(\theta_j) \tag{11}$$

Fig. 3 compares the sensitivity matrices for a single detector generated with the single ray and the volume ray-tracing methods. The single ray method exhibits spatial aliasing since neighbouring cells along the ray path can be weighted by a corner intersection and then a longer intersection, leading to a repeating cell pattern. On the other hand, the volume sampling method leads to a smoother spatial response and the sensitivity region correctly expands as you get further from the detector. Also, the toroidal geometry effects are automatically included due to the 3D nature of the calculation method.

A clear advantage of the volume sampling method is that the weight matrices are less sensitive to design tolerances. Small changes in the position and direction of a single sightline can produce quite a big difference in the aliasing pattern of the weight matrix. On the other hand, the volume ray-tracing matrix is much more stable to small perturbations in the input parameters.

Fig. 4 compares the sight line density for the whole AUG foil bolometer detector set calculated with the two methods. The sightline density matrix is the normalised sum over the k index in $\mathbf{W}$, yielding a relative measure of how well a source region l is observed relative to the other cells. For the single ray technique there are a number of cells in the plasma emission region that are effectively dark, i.e. not seen at all by a detector in the model. These cells can only be filled in by regularisation, which has consequences for plasma emission scenarios with localised emission features that overlap these regions. The volume ray-tracing method allows the solution to be constructed from a much smoother set of basis functions and should lead to a more constrained (lower spatial frequency) solution space.

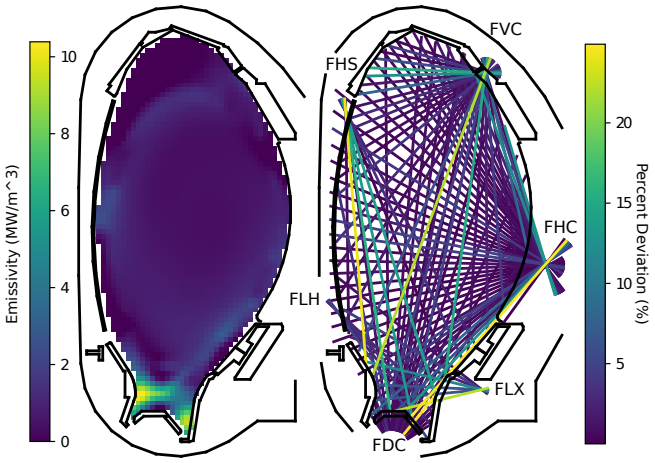

FIG. 5. Figure a) shows the BLB code inverted emission profile for AUG shot 33280 at 4.1s. Figure b) shows the forward calculated sightlines colour-coded by the percentage error between the two techniques. The bolometer camera positions are labeled.

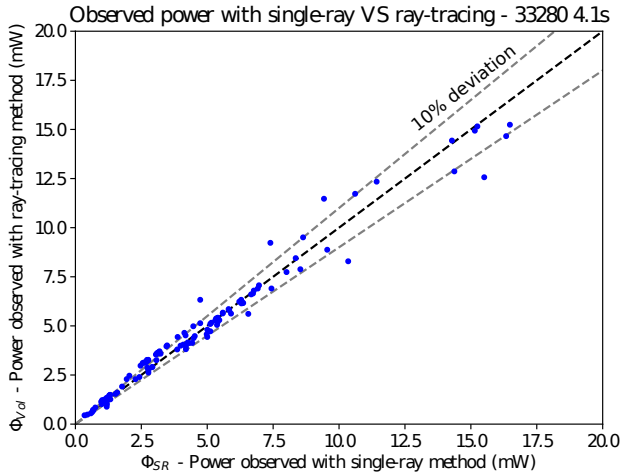

FIG. 6. Plot of the forward modelled power with the single-ray technique, Φ_{SR}, against the power calculated with ray-traced volumes, Φ_{Vol}, for each detector observing the radiation scenario in Figure 5. The deviations become more pronounced at higher powers which tends to correlate with sightlines that see the divertor.

FIG. 7. Example case where the single-ray path terminates too early on a tile surface. When the volume ray-tracing technique is used a large fraction of the collection volume extends into the inner divertor resulting in a significant error in the collected power calculation.

To study these effects further we have used an example radiation scenario from AUG shot 33280 at 4.1s inverted with the currently applied AUG tomography code[11], shown in Fig. 5 a). This tomography code uses the conventional single ray model for its inversions. Fig. 5 b) shows each sightline colour coded by the percentage error in the observed power when the single-ray approximation is used in comparison to volume ray-tracing. Similarly, Fig. 6 shows a scatter plot of the forward modelled power calculated with a single-ray, Φ_{SR}, against the power calculated with a ray-traced volume, Φ_{Vol}, for each detector.

For many detectors observing lower powers the single sight line is a good approximation, these sightlines are looking across the bulk plasma which is characterised by smoother emission gradients. However the errors can become more significant ($> 10\%$) for sightlines that see the divertor region with strong gradients, such as strike point and x-point radiation. Single ray sightlines that tend to see a locally bright source will over-estimate the power, whereas sightlines that narrowly miss a bright source (such as a strike point) will under-estimate the power. It is also possible to under-estimate the power due to occlusion effects where the single ray path terminates too early compared to the full collection volume. An example of a sightline with this characteristic is shown in Fig. 7.

V. PERFORMANCE VS PHANTOMS

To explore the differences between reconstruction results obtained using the two sensitivity matricies, the two methods were tested on a standard population of 94 phantom emission scenarios[12] used to benchmark the existing tomography code[11]. The 94 phantoms form a standard set of test cases constructed from combinations of six basic emission sources: uniform backgrounds with gradients; point sources; x-points; strike points; divertor legs; and radiation rings on a flux surface[12]. The full population of phantoms are designed to test the systems ability to resolve representative emission features that may be encountered in real plasmas.

Virtual observations for each phantom are constructed by multiplication of the sensitivity matrix with the phantom's emissivity vector, as per equation 8. In addition, 5% gaussian distributed noise was added to the virtual observations to simulate the effects of detector noise.

The population of phantoms were inverted with the Simultaneous Algebraic Reconstruction Technique (SART)[13]. The SART method is an iterative inversion scheme where the emission cells are updated with the formula

$$x_l^{(i+1)} = f_{sart}(x_l^{(i)}) = x_l^{(i)} + \frac{\omega}{W_{\oplus,l}} \sum_{k=1}^{N_d} \frac{W_{k,l}}{W_{k,\oplus}} (\Phi_k - \hat{\Phi}_k), \tag{12}$$

where

$$W_{k,\oplus} = \sum_{l=1}^{N_s} W_{k,l}, \quad W_{\oplus,l} = \sum_{k=1}^{N_d} W_{k,l}.$$

Here $x_l^{(i)}$ is the previous estimate for the emission at source l in iteration i. The relaxation hyperparameter was set to $\omega = 1$ for this study. The SART method effectively updates each cell by the weighted average error between the forward modelled $\hat{\Phi}_k$ and observed Φ_k measurements. The observed errors are weighted by both their proportion of the total ray length ($W_{k,\oplus}$) and the sum of the effective ray paths crossing that cell ($W_{\oplus,l}$).

Some common choices for regularisation of inverse problems include the l_2 norm and gradient based constraints[15]. The current AUG code employs the Anisotropic Diffusion Model Tomography[11] (ADMT) scheme, which assumes that radiation varies less along magnetic flux surfaces than perpendicular to them. The regularisation is prescribed in terms of two diffusion terms, perpendicular $D_\perp$ and parallel $D_\parallel$ to flux surfaces.

In this work we have opted for a 2D discrete Laplacian operator as the regularisation constraint[14]. Some previous studies added this reglarisation directly to the weight matrix[14], here we have linearly added the regularisation term to the update formula.

$$\hat{\mathcal{L}}(x_l^{(i)}) = \beta_L (C x_l^{(i)} - \sum_{c=1}^{C} x_c^{(i)}) \tag{13}$$

Here, c is the index for the sum over the eight possible neighbouring cells. See Figure 8 for an example of the operator in two different grid positions. The strength of the β_L hyperparameter determines the amount of local smoothness imposed. With the Laplacian constraint the update formula becomes

$$x_l^{(i+1)} = f_{sart}(x_l^{(i)}) - \hat{\mathcal{L}}(x_l^{(i)}). \tag{14}$$

In future work this term could be exchanged for the ADMT scheme.

To measure the performance of the inversions, there are a number of different distance measures that can be used. In this work, we have opted for the Pearson correlation coefficient, ρ_c, which can measure the correlation

a)
-1	-1	-1
-1	8	-1
-1	-1	-1

b)
-1		
-1	5	
-1	-1	-1

FIG. 8. Examples of the 2D Laplacian operator for a) a central cell ($C = 8$) and b) a cell near the inversion grid corner ($C = 5$).

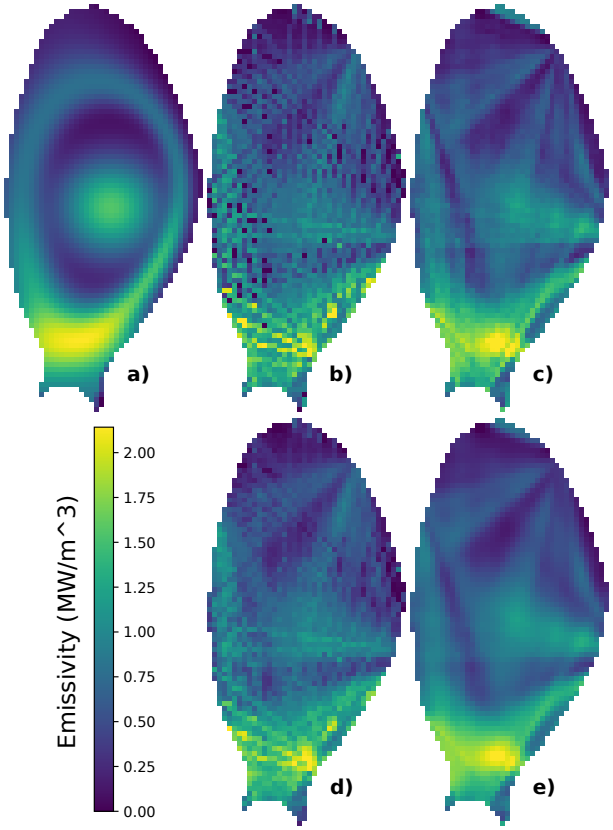

FIG. 9. Bolometer foil measurements of the phantom emission scenario given in a) have been forward modelled with the volume ray-tracing method. The synthetic measurements are then inverted with the unregularised SART algorithm using weight matrices constructed with the single-ray approximation b) and the volume ray-tracing method c). The differences between b) and c) demonstrate the extra spatial constraints imposed by volume ray-tracing. Additionally, both single-ray and ray-tracing inversions were used with regularised SART in d) and e) respectively. See Table I for a comparison of the results.

	Phantom a)	SR b)	VOL c)	SR + Reg d)	VOL + Reg e)
P_{rad} (MW)	13.82	13.37	13.76	13.45	13.7
ρ_c		0.68	0.85	0.79	0.89

TABLE I. The total radiated power, P_{rad}, and Pearson correlation coefficient, ρ_c, for each of the inversions in Figure 9. The regularised inversions have $\beta_L = 0.0125$.

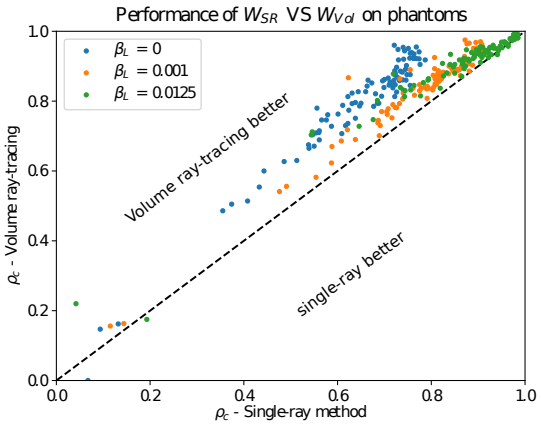

FIG. 10. Performance on all 94 phantoms of the two weight matrices, $\mathbf{W_{SR}}$ and $\mathbf{W_{Vol}}$ for varying levels of regularisation. The performance measure is the Pearson correlation coefficient, where $\rho_c = 1$ means the inverted emission profile is identical to the phantom emission profile.

between two vectors[16]. In this context it is defined as the covariance of the two emssion source vectors, inversion $\mathbf{x_{inv}}$ and phantom solution $\mathbf{x_{sol}}$, divided by the product of their standard deviations,

$$\rho_c = \frac{\mathrm{Cov}(\mathbf{x_{inv}}, \mathbf{x_{sol}})}{\sigma(\mathbf{x_{inv}})\sigma(\mathbf{x_{sol}})}. \tag{15}$$

The SART inversions were performed on all 94 phantoms with weight matrices computed with both the single-ray ($\mathbf{W_{SR}}$) and volume ray-tracing ($\mathbf{W_{Vol}}$) techniques, both with and without the Laplacian gradient regularisation. The resulting inversions for an example phantom are shown in Figure 9, with an accompanying comparison of the total radiated powers and correlation coefficients to the phantom in Table I. The differences between Fig. 9 b) and c) demonstrate the extra spatial constraints imposed by the volume ray-tracing method. The $\mathbf{W_{Vol}}$ matrix continues to outperform $\mathbf{W_{SR}}$ for the same level of gradient regularisation.

Figure 10 shows the performance on all phantoms for varying levels of regularisation. It demonstrates that the volume ray-tracing matrices are naturally more spatially constrained and require lower levels of regularisation for the same performance with single-rays. Furthermore, it is clear from Fig. 10 that turning up the regularisation is mainly affecting the single ray inversions. At higher levels of regularisation, the two distributions are in more agreement because regularisation is a property of the solution matrix, not the sensitivity matrix, and hence regularisation can dominate the solution. However, even at the highest regularisation level there is still a clear offset demonstrating the volume ray-tracing technique has superior performance.

Figure 11 shows the distribution of total radiated power for each inversion plotted against the phantom's

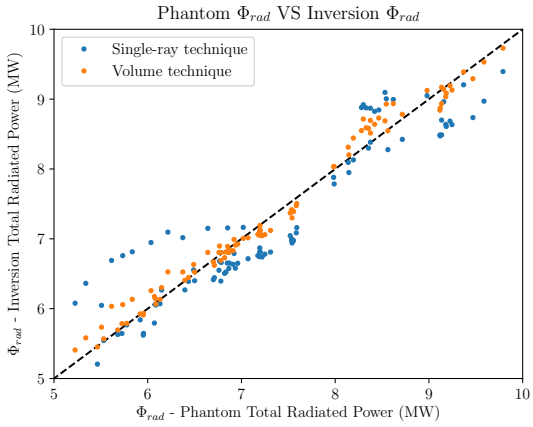

FIG. 11. The phantoms' total radiated power, Φ_{rad}, plotted against the inverted solution Φ_{rad} for all 94 phantoms using the single ray and volume ray-tracing techniques. Inversion performance decreases as the inversion points move away from the dashed line. This dataset used the middle regularisation case ($\beta_L = 0.001$) and demonstrates the volume-raytracing technique consistently out performs the single ray model.

real total radiated power. The distributions are plotted for both the single-ray and volume ray-tracing techniques using the middle regularisation case. The spread of points for the $\mathbf{W_{SR}}$ case is bigger than the $\mathbf{W_{Vol}}$ distribution and demonstrates the volume ray-tracing technique consistently out performs the single-ray model. The distribution of deviations for the single-ray technique was 5.2±4.1% compared with 1.7±1.5% for the volume ray-tracing technique.

VI. DISCUSSION

The volume ray-tracing technique is expected to have the most impact on fusion machines where the solid angle of the detectors is sufficiently large that the beam width of the detector sensitivity spans multiple plasma features or gradients. Naturally, the impact is much less when the detector's sensitivity is highly collimated compared to the inversion grid.

The volume ray-tracing approach tends to produce weight matrices where every grid cell is seen by multiple detectors. This has a natural smoothing effect on the solution matrix. The AUG bolometry system has a very high degree of spatial coverage and only ∼5% dark cells in the inversion grid. Hence, these effects could be more significant on machines such as JET with poorer spatial coverage.

Regularisation normally smooths over many sources of error in an inversion process. Using volume ray-tracing to calculate the étendue and sensitivity matrices allows us to use a more physical model of the detector response, and hence helps remove some of the systematic error sources. Therefore it is not surprising that the volume ray-tracing approach has better performance at a given level of regularisation.

However there are still other errors, such as detector noise and design errors that are always present in the data. There are also physical effects such as energy deposition/reflection of neutral particles and the finite foil reflectivity as a funciton of wavelength. The improvement due to volume ray-tracing degrades with increasing levels of noise, where higher levels of regularisaiton are required. So it is important to have a system with a high level of signal to noise to see the benefits from this technique. On the other hand, there does not appear to be any disadvantages from including the extra calculation detail in the inversions.

The ideal inversion routine would require minimum human input in terms of prior information (regularisation hyperparameters) and be computable on reasonable time scales. Typical bolometry weight matrices computed with the single-ray technique are not sufficiently constrained to produce acceptable inversions without regularisation. In contrast, the volume ray-tracing weight matrices can produce acceptable inversions ($\rho_c > 0.8$) without regularisation for a significant range of plasma scenarios. However regularisation was still required to bring the majority of the phantom population above this threshold.

In future work it may be possible to combine volume ray-tracing with a better inversion algorithm, such as bayesian Markov Chain Monte Carlo or maximum entropy techniques, to achieve an acceptable inversion routine with very few hyperparameters.

The calculations for volume ray-tracing are more computationally intensive than for a single ray, however they only need to be calculated once. Re-calculation is only required when changing the inversion grid or the detectors, which is typically between experimental campaigns.

VII. CONCLUSIONS

Volume ray-tracing techniques combined with full 3D machine models have been used to calculate the étendue and sensitivity matrices of the bolometry system at ASDEX-Upgrade. The volume ray-traced sensitivity matrices were benchmarked against sensitivity matrices calculated with the more conventional single-ray technique. The volume ray-tracing technique can include vignetting effects from other installation features not possible to include in single ray calculations.

Inversions using both matrices were carried out on a population of emission phantoms with varying levels of regularisation. The volume ray-tracing technique consistently out-performed the single-ray technique in regards to both the correlation coefficient distance measure and the accuracy of the inverted total radiation power. The volume ray-tracing technique was shown to be naturally more spatially constrained.

The technique is a useful addition to the stan-

dard bolometry techniques currently in use and doesn't present any obvious disadvantages. However, the volume ray-tracing method requires detailed in-situ information of the system and the improvement over the single-ray technique degrades quickly with increasing sources of error such as detector noise and design errors. It is important for a bolometry system to have good signal to noise ($\leq 5\%$ detector noise) to gain significant benefit from the extra calculations.

ACKNOWLEDGMENTS

The authors wish to acknowledge the contributions of V. Brack at IPP Garching who extracted the relevant bolometer camera geometry from the engineering CAD files.

This work has been carried out within the framework of the EUROfusion Consortium and has received funding from the Euratom research and training programme 2014-2018 under grant agreement No 633053 and from the RCUK Energy Programme [grant number EP/P012450/1]. The views and opinions expressed herein do not necessarily reflect those of the European Commission.

B. Lipschultz was funded in part by the Wolfson Foundation and UK Royal Society through a Royal Society Wolfson Research Merit Award as well as by the RCUK Energy Programme (EPSRC grant number EP/I501045).

[1]Reimold, F., et al. "Divertor studies in nitrogen induced completely detached H-modes in full tungsten ASDEX Upgrade." Nuclear Fusion 55.3 (2015): 033004.

[2]Ingesson, L.C. et. al. (2008). Tomography diagnostics: Bolometry and soft-x-ray detection. Fusion Science and Technology, 53(2), pp.528-576.

[3]Sheikh, U. A., et al. (2016). "A novel carbon coating technique for foil bolometers." Rev. Sci. Instrum. 87.11: 11D431.

[4]Craciunescu, T. et. al. (2009). A comparison of four reconstruction methods for JET neutron and gamma tomography. Nucl. Instrum. Methods Phys. Res. Sect. A, 605(3), pp.374-383.

[5]Ingesson, L. C., Maggi, C. F. and Reichle, R. (2000). "Characterization of geometrical detection-system properties for two-dimensional tomography." Rev. Sci. Instrum. 71.3: 1370-1378.

[6]Giroud, C., et al. (2018, March 23). "CHERAB Spectroscopy Modelling Framework (Version v0.1.0)". Zenodo. http://doi.org/10.5281/zenodo.1206142

[7]Meakins, A. and Carr, M. (2017, December 11). "Raysect Python Raytracing Package (Version v0.4.0)". Zenodo. http://doi.org/10.5281/zenodo.1205064

[8]Bernert, M., et al. (2014) "Application of AXUV diode detectors at ASDEX Upgrade." Rev. Sci. Instrum. 53.3 104003.

[9]Pharr, M. & Humphreys, G. (2016). Physically based rendering: From theory to implementation. Morgan Kaufmann.

[10]Veach, E., (1997). Robust Monte Carlo methods for lighting simulation. PhD thesis, Stanford University.

[11]Fuchs, J. C. et. al. (1994). Two dimensional reconstruction of the radiation power density in ASDEX-Upgrade. 21st Conference on Controlled Fusion and Plasma Physics, Montpellier.

[12]Glöggler, S. (2018). "Development of an Algorithm to Determine the Total Radiated Power (IPP 2018-06)". Garching: Max-Planck-Institut für Plasmaphysik. doi:10.17617/2.2564760.

[13]Andersen, A. & Kak, A. (1984). Simultaneous algebraic reconstruction technique (SART): a superior implementation of the ART algorithm. Ultrasonic imaging, 6(1), 81-94.

[14]Hobiger, T., Kondo, T., & Koyama, Y. (2008). Constrained simultaneous algebraic reconstruction technique (C-SART)a new and simple algorithm applied to ionospheric tomography. Earth, planets and space, 60(7), 727-735.

[15]Aster, R., Borchers, B. and Thurber, C. (2011). "Parameter estimation and inverse problems". Vol. 90. Academic Press.

[16]Pearson, K. "Note on regression and inheritance in the case of two parents." Proceedings of the Royal Society of London 58 (1895): 240-242.